Journal of Power Sources 196 (2011) 7302–7307

Contents lists available at ScienceDirect

Journal of Power Sources

journal homepage: www.elsevier.com/locate/jpowsour

Reconstruction of porous electrodes by FIB/SEM for detailed microstructure modeling

Jochen Joos[a,*], Thomas Carraro[b], André Weber[a], Ellen Ivers-Tiffée[a,c]

[a] Institut für Werkstoffe der Elektrotechnik (IWE), Karlsruher Institut für Technologie (KIT), Adenauerring 20b, D-76131 Karlsruhe, Germany
[b] Institut für Angewandte Mathematik(IAM), Ruprecht-Karls-Universität Heidelberg, D-62120 Heidelberg, Germany
[c] Center for Functional Nanostructures (CFN), Karlsruher Institut für Technologie (KIT), D-76131 Karlsruhe, Germany

ARTICLE INFO

Article history:
Received 1 July 2010
Received in revised form 1 October 2010
Accepted 2 October 2010
Available online 10 October 2010

Keywords:
SOFC
LSCF
Focused ion beam (FIB)
Microstructure modeling
Segmentation algorithm

ABSTRACT

Polarization losses within electrodes of solid oxide fuel cells (SOFCs) are determined both by material composition and microstructure. Improvement in performance can be supported by a detailed characterization and modeling of the electrode microstructure. Focused ion beam (FIB) and scanning electron microscopy (SEM) combined with image processing have already proven potential for the reconstruction of porous electrodes. In this contribution the serialized reconstruction procedure of a high-performance, mixed ionic-electronic conducting $La_{0.58}Sr_{0.4}Co_{0.2}Fe_{0.8}O_{3-\delta}$ (LSCF)-cathode will be illustrated in detail. Based on corrected reconstruction data sets and by the evaluation of qualified algorithms discriminating between porosity and electrode material, a sensitivity analysis of the grayscale threshold value on the essential parameters (i) surface area, (ii) volume/porosity fraction and (iii) tortuosity is performed.

1. Introduction

To accelerate the commercialization of solid oxide fuel cells (SOFCs), it is essential to improve the electrode performance over the entire temperature range between 600 and 900 °C. Mixed ionic-electronic conductors (MIECs) such as $La_{0.58}Sr_{0.4}Co_{0.2}Fe_{0.8}O_{3-\delta}$ (LSCF) are qualified as high-performance cathodes at intermediate and low operating temperatures. Polarization losses are determined both by material composition and microstructure. Improvement in performance can be supported by a detailed characterization and modeling of the electrode microstructure. High-quality, detailed microstructure-data are a prerequisite, which can be obtained by focused ion beam (FIB) and scanning electron microscopy (SEM) combined with image processing [1–6]. The FIB procedure applies Ga ions to mill thin sections from the exposed electrode surface, which is imaged at the same time by SEM. Sequential milling and imaging yield a serial set of consecutive images of the electrode. By stacking the 2D images in a 3D space (cf. Fig. 1) and aligning the pixels of the images in the slicing direction (space between two images), a 3D reconstruction of the microstructure, consisting of voxels (volumetric pixels), is derived [6].

This 3D reconstruction data set gives a valuable basis for the determination of essential microstructure parameters: (i) surface area, (ii) volume/porosity fraction and (iii) tortuosity. This combined FIB/SEM and reconstruction approach was reported recently for both SOFC anodes and cathodes by several groups [1–5]. However, the reconstructed volume elements were kept rather small and hardly representative of the entire electrode structures. Furthermore, aspects concerning the accuracy of the alignment procedure were not given in detail, but are essential for the quality of the 3D reconstruction data sets, as discussed in [7]. The unambiguous segmentation of the grayscale frequency distribution into pores and electrode material, to our understanding, is the most important step in image processing. Therefore, we will present (1) an analysis of qualified algorithms able to automatically identify a "true" threshold value and (2) discuss the variance of the resulting microstructure parameters.

2. Materials and methods

2.1. Sample preparation

The FIB/SEM procedure was applied to a high-performance LSCF cathode, which was screen-printed and sintered onto a $Ce_{0.8}Gd_{0.2}O_{2-\delta}$ (CGO) interlayer and a thin film $Y_{0.16}Zr_{0.84}O_{2-\delta}$ electrolyte (8YSZ). The entire anode supported cell (ASC) was developed at the Research Center Jülich, details of the manufacturing procedure are given in [8]. Moreover, the electrical performance of the

* Corresponding author at: Institut für Werkstoffe der Elektrotechnik (IWE), Karlsruhe Institute of Technology (KIT), D-76131 Karlsruhe, Germany.
Tel.: +49 721 6087494; fax: +49 721 6087492.
E-mail address: jochen.joos@kit.edu (J. Joos).

0378-7753/$ – see front matter © 2010 Elsevier B.V. All rights reserved.
doi:10.1016/j.jpowsour.2010.10.006

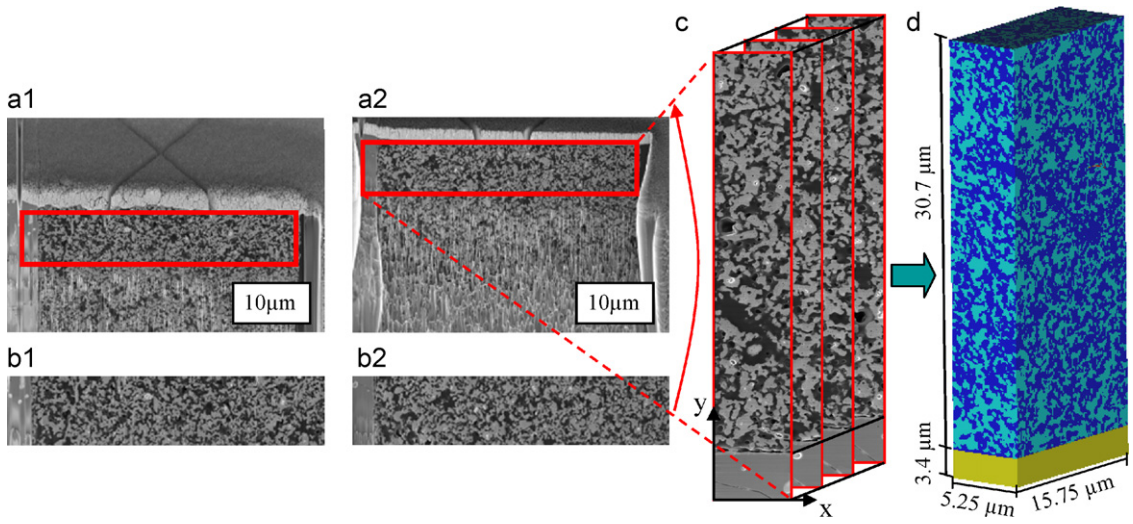

Fig. 1. SEM-images of a porous $La_{0.58}Sr_{0.4}Co_{0.2}Fe_{0.8}O_{3-\delta}$ (LSCF) cathode (a1 and a2): the usable sector (b1 and b2) of the entire image shifts upwards with increasing penetration depth in slice direction (*z*-direction). By stacking and aligning the 2D images in 3D space a detailed 3D reconstruction of the microstructure is derived (d) [6].

ASC was evaluated in the past in great detail via electrochemical impedance spectroscopy [9,10].

The sample preparation was presented in detail in a previous paper [6], nevertheless the most important issues will be repeated here. The ASC was first cut into smaller pieces of approximately 5 mm × 2 mm. Then the pores were vacuum infiltrated with a two component resin, which strengthens the porous microstructure during FIB/SEM treatment and allows for a better planar sectioning. But most important it supports the identification of the pore phase during image processing (as the resin within the pores appears as dark black, which improves the contrast with the light gray electrode material, see SEM images in Fig. 1). Hence infiltration is an essential precondition to allow an automated segmentation on the consecutive images, which will be discussed in detail later.

The edges of the sample were polished to obtain planar surfaces and sharp edges. This allows starting the process of FIB sectioning right from the edge of the sample. A gold coating (~2.5 µm thickness) was sputtered on top of the sample to protect the microstructure and help to reduce streaking [2].

2.2. FIB/SEM processing

For the sequential process of FIB milling and SEM imaging a ZEISS 1540XB CrossBeam® (Carl Zeiss AG, Oberkochen, Germany) was used. The two beams have a coincident angle of 54°, as shown schematically in Fig. 2. It is possible to run the sequential process automated, but before starting the process, it is important to find the right settings. Therefore we made some preliminary calculations concerning the accuracy of the data obtained with FIB/SEM techniques [6]. An important factor is the resolution or rather the number of pixels (respectively voxels) per particle-diameter that is necessary in the SEM images. The results [6] have shown that a resolution of at least 20–30 voxels per particle-diameter is required for the convergence of parameters like surface area or porosity. To ensure a sufficient resolution in all three directions, this holds not only for the resolution of the SEM images (resolution in *x*- and *y*-direction) but also for the slicing resolution (distance between two images, i.e., resolution in the *z*-direction). However, in most cases there is a difference between the resolution of the SEM images and the slicing distance [1–4]. This can be readjusted by applying a re-sample step on the FIB/SEM data.

2.3. 3D reconstruction

An important aspect is the estimation of the minimal volume size that has to be reconstructed for reliable and representative results. This volume size is generally named representative volume element (RVE) or stochastic equivalent representative volume element (SERVE), and this aspect was discussed in detail in [6,11,12]. Here a SERVE is employed but we use the term RVE in accordance with other publications [7,11]. Based on a coarse 3D FEM-model, described in [6,13,14], we calculated the area specific resistance of the cathode (ASR_{cat}) as a figure of merit for cathode performance. As a result the ASR_{cat} drops with increasing number of electrode particles *N* (hence with increasing contact area between cathode and electrolyte) and reaches an asymptotic limit. Logically, this limit depends on the porosity of the electrode structure considered. In the case presented, as the porosity is in between 30 and

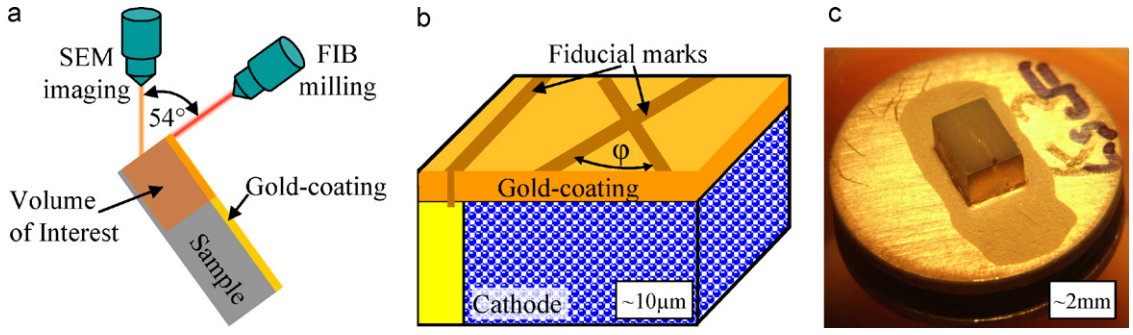

Fig. 2. (a) Schematic design of a FIB/SEM setup from the side view [3]. (b) Prepared sample and (c) the sample with the observed region of interest after FIB/SEM treatment.

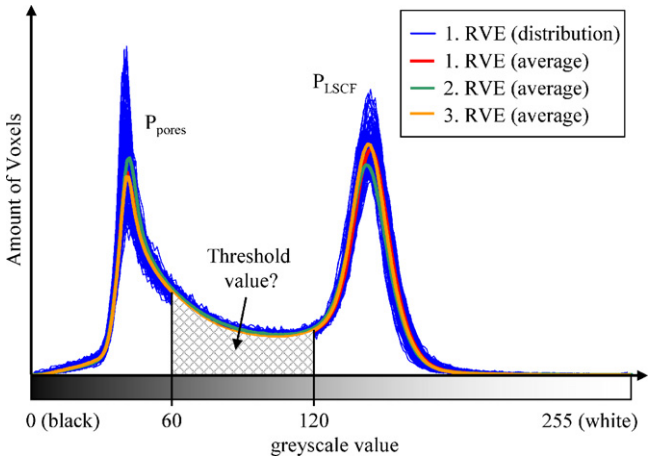

Fig. 3. Histogram of the grayscale frequency distribution of the reconstruction data: thin blue lines show the individual distributions of grayscales for each of the 213 images used for the reconstruction, while lines in red, green and ochre indicate the average values of 3 RVEs. The appropriate threshold value for the segmentation into pores and electrode material (LSCF) is located in the "valley" between the two histogram peaks.

50%, N should be >6–7 in one dimension [6]. We conclude that the volume element must cover a base area of at least 7×7 particles [6,13]. The reconstructed cathode structure shown in Fig. 1d is 30.7 μm (height) × 5.25 μm × 15.75 μm, and was assembled from almost seven hundred consecutive images.

The SEM images taken during FIB milling are usually comprised of a larger area than required for reconstruction. During FIB milling, the entire image shifts upwards with increasing penetration depth in the slicing direction (z-direction). Therefore, the usable sector for reconstruction has to be cut out of the entire image. Fig. 1 shows the SEM-images of the investigated porous LSCF-cathode (Fig. 1, Parts a1 and a2) as well as the sector used for reconstruction (Fig. 1, Parts b1 and b2). The cut-out procedure was supported by the software MATLAB (The MathWorks, Natik, MA, USA). By stacking all seven hundred 2D images in a 3D space and expanding the pixels in the third dimension (space between two images), the pixels become voxels and a 3D reconstruction is obtained. Thereupon the precise alignment of consecutive images is of outstanding importance for the resulting 3D reconstruction data set. So far, this issue was not extensively discussed in the literature. In our case, even small misalignment leads to defective information due to the high resolution of the images (pixel size of ~35 nm, image distance of ~25 nm), for more details we refer to [7].

3. Results and discussion

3.1. Threshold grayscale value

One single resulting 3D reconstruction data set, denominated as a RVE, contains 213 individual images. Consequently we could generate three non-overlapping RVEs out of seven hundred images. Every single image consists of different grayscale values, discriminated from a value of 0 (black) to a value of 255 (white). The resulting grayscale value frequency distribution of all 213 images as well as the average values of the 3 RVEs are shown in the histogram (Fig. 3). At a glance, the most significant information is extracted from the two maxima, clearly assigned to (i) pores at a mean grayscale value of ~40 and (ii) electrode material at ~144.

More precisely, the entire grayscale image, voxel by voxel, has to be unambiguously assigned either to a pore or to electrode material. This so-called segmentation, to our understanding, is the most important step in image processing and potentially a large source of error. For segmentation, the literature proposes different methods and it is even today a field of ongoing research. For the segmentation of pixel- and voxel-based data, the most common and capable method of image segmentation is thresholding [15]. The appropriate threshold value for the reconstruction is located somewhere in the "valley" between the two histogram peaks (cf. Fig. 3).

But despite its apparent simplicity, thresholding is a very powerful method but also challenging [15]. First and foremost it has to be clarified that segmentation with a threshold value is a constructive approach, followed by the allocation of the "true" threshold value. To check if an automated segmentation with a threshold value is expedient, a shape analysis of the histogram (Fig. 3) can be helpful.

A strong indication that segmentation via thresholding with one threshold value is admissible is a bimodal distribution of the grayscale values, which is obviously fulfilled here. Poor image contrast leads to a histogram where peaks tend to overlap, which makes it difficult to separate pore from electrode material. Even more serious are image shadowing artifacts [15], which lead to images that appear lighter at one side and darker at the other. Furthermore, because of the need for a reasonable number of images (here: one RVE consists of 213 images), all of them should have the same contrast. Additionally the absence of a brightness gradient between the consecutive images is a precondition. This can be controlled by comparing the individual histograms of the subsequent images. If the histogram peaks of the different images are not shifted against each other, it can be concluded that there is no brightness gradient and no image shadowing.

It can be recognized from the grayscale frequency distribution of 213 individual images (cf. Fig. 3) that the distribution of the two peaks is well aligned. As a consequence, brightness gradient or shadowing is of no concern and segmentation with a uniform threshold value is permitted. (In our case, image shadowing was avoided by an advantageous sample preparation [6], alternatively the lift-out technique can be applied [2].)

As the preconditions for segmentation by thresholding are now fulfilled, we can concentrate on the question: which grayscale value in the "valley" represents the appropriate threshold? Locating the "true" threshold value is the most important task in image processing. Fig. 4 shows two examples for a poorly chosen threshold: if the corresponding grayscale value is much too low (with a value 60 in Fig. 4a), a significant part of the pore volume is attributed to electrode material, and if the corresponding grayscale value is chosen too high (with a value of 120 in Fig. 4b), electrode material may be attributed to pore volume. It is obvious that the resulting porosity/volume fraction would be inaccurate for both cases.

The "true" threshold can be roughly allocated by interpreting the histogram shape. Given a bimodal distribution, the minimum or "valley-floor" between the peaks is the obvious choice for the threshold. In our case, where the two peaks are not clearly resolvable, several algorithms were developed during the last years. Most of them are based on statistical interpretation techniques and automatically locate the "true" threshold.

3.2. Algorithm for threshold determination

As in our histogram the peaks are not clearly resolved, respectively no clear minimum is observed (cf. Fig. 3), we evaluated several methods which automatically identify the "true" threshold value. A widely used method is the Ptile- or Median-algorithm [16]. This algorithm works well if an a-priori knowledge of the volume fraction is available. This method is obviously inadequate, as the determination of the volume fractions is one of the goals of this work. A very intuitive method for finding the appropriate threshold is the Mean-algorithm [17], which calculates the mean value of the grayscale values. This algorithm, when applied on our data set, determines a threshold value of 100.

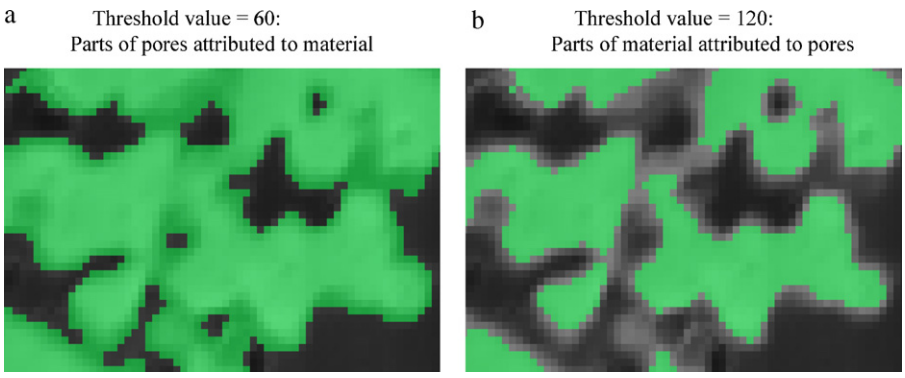

Fig. 4. Examples for a poorly chosen threshold: (a) if the threshold is chosen too low, parts of pores are attributed wrongly to electrode material (dark green regions), while (b) if the threshold is chosen too high, parts of electrode material are attributed wrongly to pores (light gray regions). (For interpretation of the references to color in this figure legend, the reader is referred to the web version of the article.)

A more advanced and one of the most qualified methods for image data consisting of two phases (pore and electrode material) is Otsu's method [18]. The two phases are considered as two clusters C_1 and C_2 of grayscale values, which are defined as

$$C_1 = \sum_{i=0}^{T} p(i) \text{ and } C_2 = \sum_{i=T+1}^{255} p(i). \quad (1)$$

The algorithm sets both clusters as tightly as possible. While adjusting the threshold value the spread of one cluster increases, whereas the other decreases. The target is then to minimize the combined spreads or equivalently maximize the variance between the clusters. First, the variances of the two clusters of intensity values, separated by an intensity threshold T, are calculated by using the mean values μ_1 and μ_2 of their grayscales:

$$\sigma_1^2 = \sum_{i=0}^{T} (i-\mu_1)^2 p(i) \text{ and } \sigma_2^2 = \sum_{i=T+1}^{255} (i-\mu_2)^2 p(i). \quad (2)$$

Second, the variance between the clusters is calculated by using the mean value of all grayscale values μ:

$$\sigma_{Bi}^2 = C_1(\mu_1 - \mu)^2 + C_2(\mu_2 - \mu)^2. \quad (3)$$

Now, the function

$$\frac{\sigma_{Bi}^2}{\sigma_T^2} \rightarrow \max \quad (4)$$

is calculated for every intensity $i = 0,\ldots,I-1$, where $\sigma_T^2 = C_1\sigma_1^2 + C_2\sigma_2^2$ is the total variance. The intensity which maximizes this function (4) is said to be the optimal threshold.

We applied the Otsu-algorithm on our image data for all three directions (x-, y- and z-plane), and came up with the "true" threshold value of 97 for all three directions. The threshold values resulting from the Otsu-algorithm (mean threshold value 97) and the Mean-algorithm (mean threshold value 100) are rather close to each other, thus the calculated porosity differs only by 1% (absolute). Nevertheless, we favor the Otsu-algorithm because this algorithm makes use of more information by calculating the variance of the two phases. Interestingly enough, we extracted the same threshold value of 97 also by "intuitive" inspection of the histogram. In the end, we performed the segmentation procedure automatically with a threshold value of 97. Thereby we fixed a porosity fraction of ~47% (47.27, see Table 1) for the porous LSCF cathode, which is on the upper boundary of what we subjectively expected beforehand. A detailed description of the quantification of microstructure parameters, as well as a sensitivity analysis on the threshold value will be given in the next section.

3.3. Quantification of microstructure parameters

From the segmented three-dimensional data, the quantification of the essential parameters (i) volume/porosity fraction, (ii) electrode surface area and (iii) tortuosity of pores and electrode material was realized. However, it seems that there is no established method to evaluate these parameters from FIB/SEM data [3]. But irrespective of the method by which the parameters were calculated, it turned out that the results depend predominantly on the chosen threshold. Fig. 5 shows the course of electrode surface area a and porosity fraction ε in dependence of threshold values varied from 60 to 100.

As expected, porosity is highly sensitive to the chosen threshold value. As discussed in the previous Section, with increasing threshold value, more and more voxels are attributed to pores, thus leading to an increase of the porosity fraction. With a threshold of 60 the porosity is clearly below 35% for all three RVEs, whereas with a threshold of 100 the porosity increased to 50%. We conclude that it is essential to establish the "true" threshold value for the calculation of the porosity/volume fraction. In contrast, the surface area is nearly insensitive to a variation in threshold value, as it varies only

Table 1
Grayscale threshold values calculated from image data by (a) the Otsu-algorithm and (b) the Mean-algorithm and the corresponding figures for porosity fraction of one RVE.

Algorithm	Threshold value	Porosity fraction, %
Mean-algorithm	100	48.50
Otsu-algorithm	97	47.27

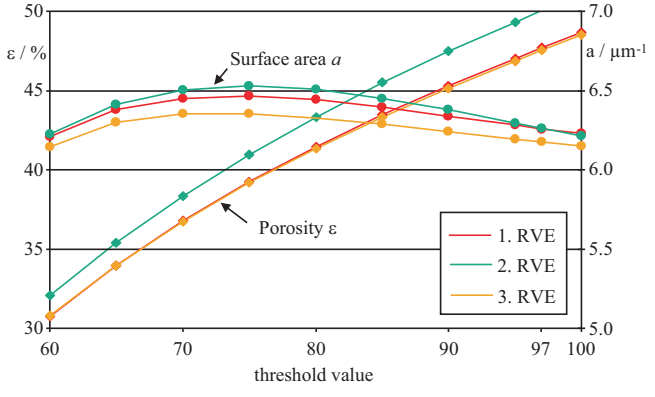

Fig. 5. Sensitivity analysis of the variance in threshold values on the microstructure parameters: (i) porosity fraction and (ii) electrode surface area, calculated with 3 RVEs.

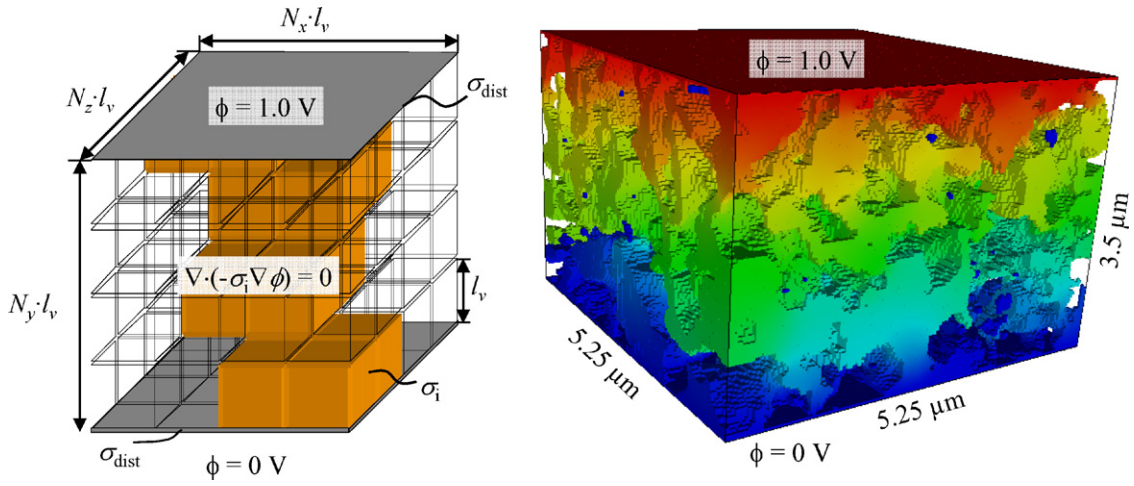

Fig. 6. Left: schematic design of the finite element method model which was applied for the calculation of the tortuosity. Right: example of the potential distribution ϕ inside the reconstructed microstructure.

in between 6.2 (μm^{-1}) and 6.5 (μm^{-1}) which is not surprising for two-phase materials.

Before calculating the tortuosity of the electrode structure, the 3D reconstruction data were re-sampled to obtain cubic voxels (35 nm × 35 nm × 35 nm). Furthermore, a finite element method (FEM) model was implemented, which has also been described in [7]. A schematic design of the model is given in Fig. 6. The tortuosity is determined in *y*-direction, from the electrolyte/cathode-interface to the current collector. On top and underneath the reconstructed volume, two thin layers with a high electrical conductivity σ_{dist} are applied to distribute and collect the current to the porous electrode structure (cf. Fig. 6). A potential difference η_{model} between these distributing layers is predefined as 1.0 V by applying a potential ϕ = 1.0 V on the upper layer and ϕ = 0 V on the bottom layer. Inside the solid phase, the transport equation:

$$\nabla \cdot (-\sigma_{bulk} \nabla \phi) = 0 \tag{5}$$

is solved to determine the current *I* that circulates through the structure. Thereby the intrinsic conductivity of the material σ_{bulk} is predefined. At the interface between the two phases, material and pore, a no-flux boundary condition was applied. Afterwards the resistance *R* of the structure is calculated by using Ohm's law. Hence the effective conductivity is given as

$$\sigma_{eff} = \frac{I}{\eta_{\mathrm{model}}} \frac{N_y}{N_x N_z l_v}, \tag{6}$$

where N_x, N_y and N_z are the number of voxels in *x*-, *y*- and *z*-direction and l_v is the edge length of the cubic voxels. Finally the tortuosity of the material (τ_{miec}) can be calculated by the formula:

$$\tau_{miec} = (1 - \varepsilon) \frac{\sigma_{bulk}}{\sigma_{eff}}, \tag{7}$$

where ε is the previously determined porosity fraction.

To determine the tortuosity of the pores (τ_{pore}), an artificial intrinsic conductivity σ_{bulk} is assigned to the pores. Therewith equation (5) is solved in the domain of the pores and analogously to the previously described method, the tortuosity of the pores is given by

$$\tau_{pore} = \varepsilon \frac{\sigma_{bulk}}{\sigma_{eff}}. \tag{8}$$

Based on this procedure, the tortuosity of the electrode material and pores was calculated for the threshold values of 70, 85 and 97 and then averaged from 3 RVEs. Given a base area of 5.25 µm × 5.25 µm, which is equivalent to 152 × 152 voxels, each of the three RVEs contains ~18.5×10^6 voxels for a height of 28 µm (which is the layer thickness of the analyzed LSCF cathode). The figure for tortuosity had been solved by parallel calculation on a high performance computer, and is summarized in Table 2.

As can be seen, the tortuosity changes from 1.66 for a threshold of 70–2.06 for a threshold of 97. One should keep in mind, that the threshold of 97 (tortuosity 2.06) was identified by the Otsu-algorithm. Clearly, the tortuosity is almost as sensitive to a variation in threshold value as the porosity. In other words, with increasing pore or electrode material fraction, the tortuosity of the contrary phase (electrode material or pore) rises.

Finally we calculated the microstructure parameters porosity, surface area and tortuosity, for a (constant) base area of 5.25 µm × 5.25 µm, but for stepwise increasing height. In other words: the reconstructed volume increases in size, starting at 1.75 µm and ending at 28 µm, which is almost the entire layer thickness of the analyzed LSCF cathode. This allows us to study a possible influence of the actual reconstruction volume on the microstructure parameters. The results are summarized in Table 3.

Consequently, for the porous LSCF structure investigated in this paper, the volume considered should take at least half of the layer thickness into account. At a thickness or height less than h < 14 µm we do not obtain a representative volume element, as the microstructure parameters quite obviously then depend on the element height *h*. This dependency disappears for larger volumes, as expected for homogeneous microstructures. In any case, the calcu-

Table 2
Average tortuosity of the electrode material and pores calculated for different threshold values (average of 3 RVE, each RVE has a reconstructed volume size of 5.25 µm × 5.25 µm × 28 µm, or ~18.5×10^6 voxels).

Threshold value (TH) (grayscale frequency distribution spans from 0 to 255)	TH 70	TH 85	TH 97 (Otsu)
Tortuosity of electrode material (LSCF) τ_{miec}	1.66	1.89	2.05
Electrode material (LSCF) fraction $(1 - \varepsilon)$, %	62.26	55.91	52.40
Tortuosity of pore τ_{pore}	2.55	2.11	1.94
Porosity fraction ε, %	37.74	44.09	47.60

Table 3
Microstructure parameters porosity, surface area and tortuosity, calculated for a (constant) base area of 5.25 μm × 5.25 μm but for increasing height (reconstructed volume has increasing size, as 28 μm is almost the entire layer thickness of the analyzed LSCF cathode) (threshold value of 97).

Height h, μm	1.75	3.5	7.0	10.5	14.0	24.5	28.0
Porosity fraction ε, %	48.91	47.87	47.82	47.65	47.81	47.34	47.27
Surface area a, μm^{-1}	6.597	6.674	6.656	6.502	6. 388	6.276	6.308
Tortuosity of MIEC τ_{miec}	1.954	1.939	1.950	1.969	1.989	1.989	1.985
Tortuosity of pore τ_{pore}	2.039	1.983	1.975	1.979	1.959	1.964	1.967

lations must be solved by parallel calculation on a high performance computer.

4. Conclusions

The microstructure of porous electrodes can be assessed only if accurate data on grain size, porosity, tortuosity, etc. are available. For this purpose, a serialized reconstruction procedure for FIB/SEM derived 3D microstructure data of a high-performance, mixed ionic-electronic conducting $La_{0.58}Sr_{0.4}Co_{0.2}Fe_{0.8}O_{3-\delta}$ (LSCF)-cathode, was developed.

During the entire reconstruction process numerous sources of error can occur (see [6,7]) but in this contribution we focused on the section of image processing. Herein, the unambiguous segmentation of the grayscale frequency distribution into pores and electrode material, to our understanding, is the most important step. Therefore, an analysis of two qualified algorithms (Otsu, Mean) capable of automatically identifying a "true" grayscale threshold value was performed. In case of a bimodal (here: pores and electrode material) frequency distribution, Otsu's method was marginally preferred. Furthermore the variance of the parameters: (i) surface area, (ii) volume/porosity fraction and (iii) tortuosity depending on the threshold value were calculated. Whereas porosity as well as tortuosity varies strongly with the threshold value, the surface area is almost constant between porosities of 35 and 50%. For the given LSCF electrode structure, a "true" threshold of 97 (among a grayscale variation from 0 (black: pore) to 255 (white: electrode material) was identified. The microstructure parameters were identified as (i) surface area 6.3 (μm^{-1}), (ii) porosity fraction 47.3% and (iii) tortuosity of pore 1.97.

Part of the results could only be extracted from a newly developed 3D FEM-model, which can cope with a large number of voxels (10^7 to 10^8). It contains a solver based on high performance computing techniques, and a 3D stochastic geometry generator. Further details on this 3D numerical model will be the subject of a forthcoming article.

Acknowledgements

The authors gratefully acknowledge Dr. Bernd Rüger for his invaluable and continuous support to this work. Dr. Heike Störmer from the Laboratory for Electron Microscopy, Karlsruher Institut für Technologie (KIT) is acknowledged for the preparation of the LSCF-cathode. Moreover, the continuous discussion with the group of Prof. Dr. Schmidt, Institut für Stochastik, Universität Ulm, has substantially supported our research work. This work was funded by the Friedrich-und-Elisabeth-BOYSEN-Stiftung and by the Deutsche Forschungsgemeinschaft (DFG) through project "Modellierung, Simulation und Optimierung der Mikrostruktur mischleitender SOFC-Kathoden" (IV 14/16-1). Further support by the DFG through the Center for Functional Nanostructures (CFN) within project F2.2 (former D7.2) and by the DFG projects "Nanostructured Ionic Materials: Impact on Properties and Performance" (GE 841/18-2 and IV 14/12-3) is gratefully acknowledged.

References

[1] J.R. Wilson, W. Kobsiriphat, R. Mendoza, H.Y. Chen, J.M. Hiller, D.J. Miller, K. Thornton, P.W. Voorhees, S.B. Adler, S.A. Barnett, Nature Materials 5 (2006) 541–544.
[2] P.R. Shearing, J. Golbert, R.J. Chater, N.P. Brandon, Chemical Engineering Science 64 (2009) 3928–3933.
[3] H. Iwai, N. Shikazono, T. Matsui, H. Teshima, M. Kishimoto, R. Kishida, D. Hayashi, K. Matsuzaki, D. Kanno, M. Saito, H. Muroyama, K. Eguchi, N. Kasagi, H. Yoshida, ECS Transactions 25 (2009) 1819–1828.
[4] J.R. Wilson, M. Gameiro, K. Mischaikow, W. Kalies, P.W. Voorhees, S.A. Barnett, Microscopy and Microanalysis 15 (2009) 71–77.
[5] D. Gostovic, J.R. Smith, D.P. Kundinger, K.S. Jones, E.D. Wachsman, Electrochemical and Solid State Letters 10 (2007) B214–B217.
[6] B. Rüger, J. Joos, T. Carraro, A. Weber, E. Ivers-Tiffée, ECS Transactions 25 (2009) 1211–1220.
[7] J. Joos, B. Rüger, T. Carraro, A. Weber, E. Ivers-Tiffée, ECS Transactions 28 (2010) 81–91.
[8] H.P. Buchkremer, U. Diekmann, D. Stöver, Proceedings of the 2nd European Solid Oxide Fuel Cell Forum, vol. 1, 1996, pp. 221–228.
[9] C. Endler, A. Leonide, A. Weber, F. Tietz, E. Ivers-Tiffee, Journal of Electrochemical Society 157 (2010) B292–B298.
[10] A. Leonide, V. Sonn, A. Weber, E. Ivers-Tiffée, Journal of Electrochemical Society 155 (2008) B36–B41.
[11] T. Kanit, S. Forest, I. Galliet, V. Mounoury, D. Jeulin, International Journal of Solids and Structures 40 (2003) 3647–3679.
[12] R. Hill, Journal of the Mechanics and Physics of Solids 11 (1963) 357–372.
[13] B. Rüger, Mikrostrukturmodellierung von Elektroden für die Festelektrolytbrennstoffzelle, Universitätsverlag Karlsruhe, Karlsruhe, 2009 (in German).
[14] B. Rüger, A. Weber, E. Ivers-Tiffée, ECS Transactions 7 (2007) 2065–2074.
[15] L. O'Gorman, M.J. Sammon, M. Seul, Practical Algorithms for Image Analyses, Cambridge University Press, 2008.
[16] W. Doyle, Journal of the ACM 9 (1962) 259–267.
[17] C.A. Glasbey, Computer Visions, Graphics and Image Processing 55 (1993) 532–537.
[18] N. Otsu, IEEE Transactions of the System, Man and Cybernetics 9 (1979) 62–66.